Observation of hydrodynamic modulation of gravity-capillary waves by dominant gravity waves

Tetsu Hara,[1] Kurt A. Hanson,[1] Erik J. Bock,[2] and B. Mete Uz[1]

Received 13 August 2001; revised 15 February 2002; accepted 15 October 2002; published 12 February 2003.

[1] Accurate evaluation of the hydrodynamic modulation of short wind waves by dominant gravity waves is needed for various applications of microwave radar remote sensing of the ocean surface. Such knowledge is also essential for the studies of wind wave coupling and air–sea momentum/energy transfer. Here, we present direct field observations of the hydrodynamic modulation transfer function (MTF) during two field programs (High-Resolution Remote Sensing Experiment (High-Res) off Cape Hatteras, June 1993, and Coastal Ocean Processes (CoOP) experiment off the California coast, April and May 1995). Gravity-capillary wave spectra were obtained using a scanning laser slope gauge (SLSG) for wave numbers between 25 and 800 rad m^{-1}. An array of capacitive wave wires and a motion detection package were used for the measurement of surface gravity waves. These instruments were mounted on a research catamaran, which was towed to the side of a research vessel. The observations were mostly made under low wind conditions. The observed coherence is mostly below 0.1, suggesting that the modulation of short wind waves is not strongly correlated with dominant gravity waves. The coherence is slightly higher for wave numbers 50–100 rad m^{-1} than for wave numbers above 200 rad m^{-1}. When wind and dominant waves are aligned and the water surface is clean, the magnitude of the hydrodynamic MTF is around 2–4 and its phase is close to 0. When surfactants are present and short wind wave spectra are reduced, the MTF magnitudes become significantly larger for wave numbers above 200 rad m^{-1}. When wind and dominant waves are not aligned, the coherence becomes lower as expected. The results from the two field experiments are roughly consistent with each other. The existing relaxation model may predict the hydrodynamic MTF values that are roughly consistent with the observations if the effect of modulated wind stress over gravity waves is included. *INDEX TERMS:* 4504 Oceanography: Physical: Air/sea interactions (0312); 4506 Oceanography: Physical: Capillary waves; 4560 Oceanography: Physical: Surface waves and tides (1255); *KEYWORDS:* hydrodynamic modulation, wind waves, gravity-capillary waves, gravity waves, surface waves

Citation: Hara, T., K. A. Hanson, E. J. Bock, and B. Mete Uz, Observation of hydrodynamic modulation of gravity-capillary waves by dominant gravity waves, *J. Geophys. Res.*, *108*(C2), 3028, doi:10.1029/2001JC001100, 2003.

1. Introduction

[2] Short wind waves influence various air–sea interaction processes, including air–sea exchange of energy, momentum and gas. They also play an important role in the radar remote sensing of the ocean since they contribute to the backscatter of microwave signals from the water surface. Over the open ocean, short wind waves always coexist with longer gravity waves. Their spectral density is modified by the orbital velocity of the long waves and by the modulated wind stress over the long waves. If the gravity waves are not too steep, the modulation of the short wind wave spectrum is assumed to correlate linearly with the wave height or the orbital velocity of the gravity wave; the linear transfer function between them is called hydrodynamic modulation transfer function ("hydrodynamic MTF"). The proper evaluation of the hydrodynamic MTF is important for various applications of microwave radar remote sensing, including ocean surface wave measurements by a synthetic aperture radar (SAR) [*Plant*, 1989].

[3] Existing theories of the hydrodynamic MTF are all based on the relaxation theory, that is, a perturbed short wave spectrum is assumed to approach to its local equilibrium over a relaxation timescale. The relaxation rate is normally assumed to be related to the wave growth rate due to wind. The earlier theories focused on short wave modulation due to orbital velocities of long waves [e.g., *Keller and Wright*, 1975; *Alpers and Hasselmann*, 1978] and predicted that the hydrodynamic MTF magnitude decreases as the relaxation timescale decreases (i.e., as wind speed increases). Later the importance of the modulation of wind

[1]Graduate School of Oceanography, University of Rhode Island, Narragansett, Rhode Island, USA.
[2]Interdisciplinary Center for Scientific Computing (IWR), University of Heidelberg, Heidelberg, Germany.

0148-0227/03/2001JC001100$09.00

shear stress along the long wave profile was suggested in order to explain observed relatively large hydrodynamic MTF magnitude at high winds [e.g., *Wright et al.*, 1980; *Smith*, 1986; *Hara and Plant*, 1994; *Romeiser et al.*, 1994]. Recently, *Kudryavtsev et al.* [1997] proposed a theoretical model of the hydrodynamic MTF that included the positive feedback mechanism between the modulated short wind waves and the modulated wind flow above. According to their model, more short waves give rise to a larger roughness, which increases the local stress and stimulates further growth of the short waves.

[4] Most of the past observational studies of the hydrodynamic MTF have been made using microwave backscatter from the ocean surface. At intermediate incidence angles, the radar backscatter from the ocean surface is assumed to be caused by Bragg scattering, that is, geometric resonance between electromagnetic waves and surface waves. The backscattered power is proportional to the wave number spectrum of wind waves whose wave number vector matches the Bragg resonance condition. If Bragg waves are simply riding on and modulated by large gravity waves whose wavelength is much larger than the radar footprint, the two-scale composite surface model may be applicable [*Keller and Wright*, 1975]. According to the model the modulation of the radar backscatter (total MTF) consists of three contributions, namely, the hydrodynamic MTF, the tilt MTF (caused by the modulation of the Bragg wave number), and the range MTF (caused by the modulation of the distance between the radar and the ocean surface). Therefore, the estimation of the hydrodynamic MTF must be carried out by subtracting the tilt MTF and the range MTF from the total MTF.

[5] Based on the two-scale composite surface model, *Hara and Plant* [1994] have estimated hydrodynamic MTF values using radar observations during two different field programs. They report significant differences of the hydrodynamic MTF values from the two experimental sites and speculate that different degrees of surface contamination are the source of the observed difference. They also show that the estimated hydrodynamic MTF values differ significantly between HH and VV polarizations of the radar, suggesting that the simple two-scale composite surface model is not sufficient for the estimation of the hydrodynamic MTF. This polarization dependence has been theoretically explained by *Romeiser and Alpers* [1997], who have introduced an improved composite surface model including all waves that are long compared to the Bragg waves. *Hauser and Caudal* [1996] have estimated the hydrodynamic MTF by combining the observations obtained by real-aperture radars at various incidence angles. Their results yield the magnitude of the hydrodynamic MTF that is several times larger than theoretical values and 1.5–2.5 times larger than experimental values reported in previous studies. They also point out the significant influence of the wind wave angle on the phase of the hydrodynamic MTF.

[6] One of the problems associated with the previous observations of the hydrodynamic MTF using radar backscatter is that the removal of the geometric effects from the observed total MTF is not straightforward. This procedure requires a precise knowledge of the wave number spectrum of short wind waves. If the effect of intermediate waves are included [*Romeiser and Alpers*, 1997] the estimation of the hydrodynamic MTF becomes further complicated. Another problem associated with radar observations is that such observations do not allow estimation of the coherence of the hydrodynamic MTF. It is expected that short wind waves are modulated not only by surface gravity waves but also by varying winds (wind gusts) that are not correlated with long-wave fields. This effect, in addition to the nonlinearity of the modulation process itself, reduces the coherence of the hydrodynamic MTF. With radar observations alone, this issue cannot be addressed, since the geometric effects tend to increase the coherence of the total (observed) MTF even if the coherence of the hydrodynamic MTF is low.

[7] During recent field programs we obtained the hydrodynamic MTF directly without relying on radar observations. Gravity-capillary wave spectra were obtained using a scanning laser slope gauge (SLSG) for wave numbers between 25 and 800 rad m^{-1}. An array of capacitive wave wires and a motion detection package were used for the measurement of surface gravity waves. These instruments were mounted on a research catamaran that was towed to the side of a research vessel. Here, we present the results of the direct field observations of the hydrodynamic MTF. In sections 2–5, experimental methods and the calculation of the hydrodynamic MTF are summarized. The results and discussions are given in section 6. The results are then compared with predictions using the existing relaxation theory in section 7. Finally, concluding remarks are given in section 8.

2. Experiment Summaries

[8] Most of the observations made for this study were obtained during the Coastal Ocean Processes (CoOP) experiment of April and May 1995. This experiment was funded by the National Science Foundation to investigate the role of ocean surface processes in air–sea gas exchange. This multivessel experiment was conducted in the coastal waters near California. Several research platforms were operated from the R/V *New Horizon*, including a research catamaran. The catamaran was equipped with an electric motor and a remotely controlled rudder, and was towed from the port side (about 2/3 the total ship length from the bow) of the R/V *New Horizon*. Its position was maintained at a distance of about 20 m to the side of the ship in order to minimize wind blockage and operate outside of the ship's wake. The tow speed was mostly between 0.5 and 1 m s^{-1}. A number of surface processes were studied from this platform. Gravity-capillary waves were measured using a SLSG developed by *Bock and Hara* [1995]. An array of six capacitive wave wires and a motion detection package were used for the measurement of surface gravity waves. The motion detection package recorded the motion of the catamaran. It consisted of a three-axis accelerometer and a three-axis angular rate sensor. Although gravity-wave height could be estimated with only one wave wire, an array of wave wires was deployed to allow the estimation of the directional spectrum of gravity waves [*Hanson et al*, 1997]. In addition, a hot-film sensor was placed at about 1 m depth to quantify currents and turbulence, and the study of surface chemistry was made possible by taking microlayer water samples with a surface skimmer [*Bock et al.*,

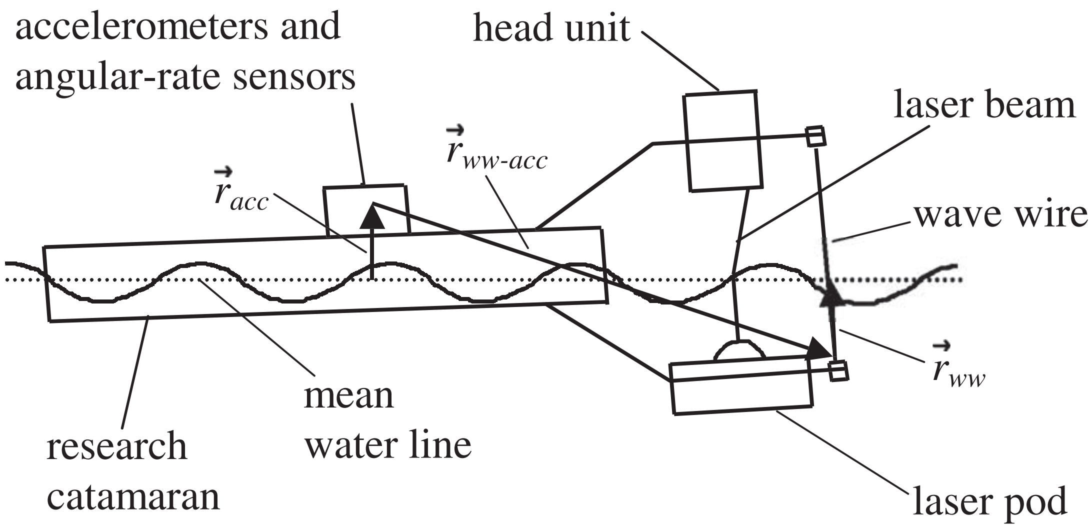

Figure 1. Schematic of the research catamaran.

1995]. Wind stress estimates were made using a three-axis sonic anemometer mounted at a height of 10 m on a bow mast aboard the R/V *New Horizon*. The stress estimates used in this paper were derived from the bulk aerodynamic method described by *Fairall et al.* [1996].

[9] Additional data utilized in this study came from the High-Resolution Remote Sensing Experiment (High-Res 2) of June 1993. This was a 21 day cruise near North Carolina sponsored by the Office of Naval Research and Naval Research Laboratory. Its purpose was to study the accuracy of microwave radar in measuring submesoscale ocean surface processes. The research catamaran was deployed from the R/V *Iselin* in a way similar to that of CoOP. It provided a means for in situ measurement of the same processes that were viewed by radar. As in CoOP, gravity-capillary waves and gravity waves were measured with the SLSG and the combination of capacitive wave wires and the motion detection package. Near-surface atmospheric winds and turbulence were measured with sonic anemometers mounted on the R/V *Iselin* and on the research catamaran.

3. Calculation of Gravity-Wave Height

[10] The wave height of swell and dominant wind waves was estimated using a suite of instruments aboard the research catamaran: a capacitive wave wire, a three-axis accelerometer, and a three-axis angular rate sensor, shown in the schematic of Figure 1. The procedure for estimating wave height from a moving platform is discussed in detail by *Hanson et al* [1997]. Therefore, this section is a brief summary of that procedure. Wave height is expressed in terms of three position vectors: $\vec{r}_{ww}$, the vector from the base of the wave wire to its intersection with the ocean surface; $\vec{r}_{ww-acc}$, the vector from the accelerometers to the base of the wave wire; and $\vec{r}_{acc}$, the position of the accelerometers relative to the mean sea surface. Wave height η is the sum of the vertical components of $\vec{r}_{ww}$, $\vec{r}_{ww-acc}$, and $\vec{r}_{acc}$, denoted by η_{ww}, η_{ww-acc}, and η_{acc}, respectively:

$$\eta = \eta_{ww} + \eta_{ww-acc} + \eta_{acc}. \quad (1)$$

The heights η_{ww}, η_{ww-acc}, and η_{acc} are derived from the wave wire, the angular rate sensors, and the accelerometers, respectively. The wave wire and accelerometers, however, acquire measurements in a reference frame with axes (x, y, z) affixed to the catamaran that continuously rotates due to gravity waves. Here, x is in the forward direction, z is vertically upward, and y is determined according to the right-hand rule. In order to determine the true vertical wave height (1), these measurements must be first transformed into a nonrotating frame with axes (x_c, y_c, z_c). A transformation matrix provides the relationship between the two reference frames. It is composed of three angles ϕ, θ, and ψ which refer to rotations about the x, y, and z axes, respectively. The motion of the research catamaran at sea results in rotation angles which are small (up to about 4° for ϕ and θ and 9° for ψ). When the angles are small, the transformation matrix becomes approximately independent of the order of the axis rotations. The angles ϕ, θ, and ψ are computed through integration of the angular rate signals.

[11] The wave height (1) is obtained as follows. The accelerometer signals are transformed to the nonrotating frame and the vertical component is integrated twice, yielding η_{acc}. The component η_{ww-acc} is the vertical component of $\vec{r}_{ww-acc}$ in the nonrotating frame, and $\vec{r}_{ww-acc}$ is computed using the angles ϕ and θ. The wave wire measures $|\vec{r}_{ww}|$ in the rotating frame. Under the small-angle approximation, η_{ww} is identical to $|\vec{r}_{ww}|$.

[12] The accuracy of the wave height results is discussed at length by *Hanson et al.* [1997]. We may express wave height in the frequency domain using standard spectral techniques. Wave height spectra in the range between 0.08 and 0.3 Hz contain errors less than 10% based on instrument errors and the accuracy of the transformation matrix. The results in this frequency range have been further verified during the High-Res 2 experiment by comparison with independent buoy measurements. Therefore, the MTF calculations are also performed in the same frequency range.

4. Measurement of Gravity-Capillary Wave Slope Spectrum

[13] The SLSG was used to measure gravity-capillary wave slope [*Bock and Hara*, 1995]. This device has two

components: a laser pod located at about 1 m depth and a head unit about 0.5 m above the water surface. The laser pod emits a rotating laser beam, which is refracted at the water surface and collected in the head unit. The rotating beam traverses a circular scan of a 0.15 m diameter on the water surface. The beam enters the head unit and is detected by two pairs of photodiodes that are used to measure wave slope components s_x and s_y. Wave slope is measured at 150 (235 during High-Res 2) locations around the scan, and one scan is completed in 2.4×10^{-3} s. In order to limit data volume, only every fourth scan is recorded at a sampling rate of 104 Hz (38 Hz during High-Res 2). The slopes are measured in the rotating reference frame (x, y, z) affixed to the research catamaran. However, the motion of the catamaran at frequencies corresponding to gravity-capillary waves is negligible. Thus, the representation of gravity-capillary waves in the rotating reference frame (x, y, z) is essentially identical to their representation in the nonrotating frame (x_c, y_c, z_c).

[14] With the CoOP data two quantities related to gravity-capillary wave slope are calculated in this study: one is the slope wave number spectrum $S(k)$ and the other is the mean square slope r. Their computation involves several steps. First the autocorrelation of surface slope $\vec{s} = (s_x, s_y)$ is computed:

$$Z(\xi, \zeta, \tau) = \langle \vec{s}(x, y, t) \cdot \vec{s}(x + \xi, y + \zeta, t + \tau) \rangle, \qquad (2)$$

where (ξ, ζ) is the spatial lag separating two scan locations and τ is the time lag. The brackets $\langle\ \rangle$ denote averaging over time. The cross correlation is transformed to the one-sided three-dimensional wave number frequency slope spectrum according to

$$S(k, \alpha, \omega) = \frac{1}{4\pi^3} \int \int \int Z(\xi, \zeta, \tau) e^{-i(k\xi \cos \alpha + k\zeta \sin \alpha - \omega\tau)} d\xi d\zeta d\tau \qquad (3)$$

which is defined for $0 < k < \infty$, $-\pi/2 < \alpha < \pi/2$, and $-\infty < \omega < \infty$. Here, k is the wave number, α is the wave propagation direction, and ω is the angular frequency. In practice, the time/frequency portion of (2) and (3) is computed using the Fourier transform of 128-point Hann-windowed time blocks. The slope wave number spectrum is found by integrating $S(k, \alpha, \omega)$ over frequency and propagation angle:

$$S(k) = \int_{-\infty}^{\infty} \int_{-\pi/2}^{\pi/2} S(k, \alpha, \omega) d\alpha d\omega \qquad (4)$$

In practice, this integration must be performed after the sidelobe contamination is removed (see the study of *Bock and Hara* [1995] for details).

[15] We examine $S(k)$ at five wave number values k = {50, 100, 200, 400, 700} rad m^{-1}. In order to reduce the statistical random error we have taken the averaging over the following wave number ranges {50, 100 ± 25, 200 ± 50, 400 ± 100, 700 ± 100} rad m^{-1}, respectively. Mean square slope r is computed by integrating $S(k)$ over wave number k

$$r = \int S(k) k dk, \qquad (5)$$

where we choose to integrate over the range of wave numbers of $100 < k < 800$ rad m^{-1}. Estimates of $S(k)$ and r are obtained for each 128-point time block, and each time block overlaps adjacent blocks by half. This yields a sampling rate for $S(k, t)$ and $r(t)$ of 1.6 Hz.

[16] High-Res 2 data are used to calculate time series of short-wave mean square slope ($r(t)$) only. The procedure for computing the mean square slope of short waves involves several steps. First, the time series of s_x and s_y at each sampling location along the scan are high-pass filtered with a cutoff frequency of 10 Hz. This step removes the wind wave energy below wave numbers 50–100 rad m^{-1} [*Hara et al.*, 1998] and the low-frequency catamaran motions from the slope time series. Next, the slope magnitude s at each location is computed according to

$$s(\vec{x}, t) = \sqrt{s_x^2(\vec{x}, t) + s_y^2(\vec{x}, t)},$$

where $\vec{x}$ is the position vector of a particular scan location and t is time. Finally, mean square slope estimates r are given, according to

$$r = \frac{1}{MN} \sum_{m=1}^{M} \sum_{n=1}^{N} s^2(\vec{x}_m, t_n), \qquad (6)$$

where m and n are the spatial and temporal indices, respectively, $M = 235$ is the number of locations around the scan, and $N = 18$ is the number of discrete times t_n used in the average. These estimates of mean square slope r are computed over contiguous time blocks, yielding a sampling frequency of 2.1 Hz for $r(t)$.

5. Estimation of Gravity-Capillary Wave Modulation

[17] The modulation of gravity-capillary waves by gravity waves may be quantified using the time series of gravity-wave height $\eta(t)$ and the gravity-capillary wave spectra $S(k, t)$. The hydrodynamic MTF is a normalized version of the cross-spectrum $C_{S_\eta}(k, f_o)$ between $S(k, t)$ and $\eta(t)$

$$M(f, k) = \frac{1}{\kappa \overline{S}(k)} \frac{C_{S\eta}(k, f_o)}{C_{\eta\eta}(f_o)}. \qquad (7)$$

Here, f_o is the observed gravity-wave frequency, f is the corresponding intrinsic gravity-wave frequency, k is the gravity-capillary wave number, $C_{\eta\eta}$ is the autospectrum of gravity-wave height η, and κ is the gravity-wave wave number corresponding to f according to the linear dispersion relation,

$$\kappa = (2\pi f)^2 g^{-1}, \qquad (8)$$

where g is the acceleration due to gravity, 9.81 m s^{-2}. The term $\overline{S}(k)$ is the mean of $S(k, t)$ over the length of the time series used in the computation of $M(f, k)$. The intrinsic frequency f and the wave number κ of gravity waves are estimated by assuming that all gravity waves are propagating in the same direction. When the catamaran velocity has a component U_{rel} in the direction θ_{rel} relative to the peak wave propagation direction, the Doppler-shifted dispersion relation becomes:

$$2\pi f_o = 2\pi f - U_{\rm rel}(2\pi f)^2 g^{-1}\cos\theta_{rel}. \tag{9}$$

The MTF $M(f, k)$ is a complex quantity. Its magnitude corresponds to the level of modulation and its phase ϕ_M gives the location of the maximum modulation of gravity-capillary waves relative to the phase of the gravity wave. Positive phase indicates that the location of maximum modulation *leads* the crest of the gravity wave. The hydrodynamic MTF for the mean square slope of gravity-capillary waves is defined similarly

$$M(f) = \frac{1}{\kappa\bar{r}}\frac{C_{r\eta}(f_o)}{C_{\eta\eta}(f_o)}, \tag{10}$$

where $C_{r_\eta}(f_o)$ is the cross spectrum between gravity-wave height $\eta(t)$ and the mean square slope time series $r(t)$. The term $\bar{r}$ is the time mean of the mean square slope time series.

[18] The degree of correlation between the gravity-capillary wave spectrum and the gravity-wave height is described by the coherence function:

$$\gamma^2(f,k) = \frac{|C_{S\eta}(k,f_o)|^2}{C_{\eta\eta}(f_o)C_{SS}(f_o)}, \tag{11}$$

where $C_{SS}(f_o)$ is the autospectrum of the gravity-capillary wave slope spectrum $S(k, t)$. The coherence may also be expressed for the mean square slope of gravity-capillary waves

$$\gamma^2(f) = \frac{|C_{r\eta}(f_o)|^2}{C_{\eta\eta}(f_o)C_{rr}(f_o)}, \tag{12}$$

where $C_{rr}(f_o)$ is the autospectrum of the mean square slope $r(t)$.

[19] The 95% confidence levels of the estimates are roughly given as

$$\hat{a}(1-2\epsilon) \le a \le \hat{a}(1+2\epsilon) \tag{13}$$

where $\hat{a}$ is the estimated value, a the true value, and ϵ the normalized random error. The estimate of ϵ is given as

$$\epsilon(|\hat{M}|) = \left(\frac{1-\gamma^2}{2\gamma^2 n_d}\right)^{\frac{1}{2}} \tag{14}$$

for the magnitude of the MTF,

$$\epsilon\left(|\hat{\phi}_M|\right) = \frac{\epsilon(|\hat{M}|)}{\phi_M} \tag{15}$$

for the phase ϕ_M of the MTF, and

$$\epsilon(\hat{\gamma}^2) = \left[\frac{2(1-\gamma^2)}{\gamma^2 n_d}\right] \tag{16}$$

for the coherence of the MTF, where n_d is the number of averaging [*Hara and Plant*, 1994]. It should be noted that these are crude estimates of the confidence levels, since the number of averaging n_d is not very large.

[20] Our calculation of the slope wave number spectrum time series $S(k, t)$ contains statistical random noise because the ensemble averaging in the correlation function (2) is finite. Random noise in the estimate of $S(k, t)$ does not affect the estimate of the cross spectrum $C_{S_\eta}(k, f_o)$, hence, it does not affect the hydrodynamic MTF $M(f, k)$. This noise does, however, increase the level of the autospectrum $C_{SS}(f_o)$, and thus it reduces the coherence $\gamma^2(f, k)$. Therefore, it is necessary to estimate the contribution of the random noise to the autospectrum $C_{SS}(f_o)$ in order to obtain true coherence values. We may achieve this by using two different spectral estimates $S(k, t)$ and $S_h(k, t)$. The latter function is computed in a manner identical to $S(k, t)$ with one exception: only half of all possible spatial lags are used in the computation of $Z(\xi, \zeta, \tau)$ of (2). Therefore, there are roughly half as many statistical degrees of freedom associated with $S_h(k, t)$. The autospectra of $S(k, t)$ and $S_h(k, t)$, denoted $C_{SS}(k, f_o)$ and $C_{hSS}(k, f_o)$, respectively, have a component corresponding to the true spectrum plus a noise component,

$$\begin{aligned} C_{SS}(k,f_o) &= C^p_{SS}(k,f_o) + C^n_{SS}(k,f_o) \\ C_{hSS}(k,f_o) &= C^p_{SS}(k,f_o) + C^n_{hSS}(k,f_o). \end{aligned} \tag{17}$$

Here, $C^n_{SS}(k, f_o)$ and $C^n_{hSS}(k, f_o)$ are the noise components of $C_{SS}(k, f_o)$ and $C_{hSS}(k, f_o)$, respectively, and $C^p_{SS}(k, f_o)$ is the true spectrum. According to the statistical theory, the noise component $C^n_{hSS}(k, f_o)$ is approximately twice of $C^n_{SS}(k, f_o)$,

$$C^n_{hSS}(k,f_o) \simeq 2C^n_{SS}(k,f_o). \tag{18}$$

Therefore, we may solve for the noise contribution as

$$C^n_{SS}(k,f_o) \simeq C_{hSS}(k,f_o) - C_{SS}(k,f_o). \tag{19}$$

We have inspected the noise spectrum $C^n_{SS}(k, f_o)$ in detail. At lower gravity-capillary wave numbers of $k = 50$ and 100 rad m^{-1}, the noise contribution $C^n_{SS}(k, f_o)$ is about 20–30% of $C_{SS}(k, f_o)$. Therefore, the true coherence is estimated to be about 1.3–1.4 times the estimate given by (11). At higher wave numbers $k > 200$ rad m^{-1}, the noise contribution is at most 10%, hence, the true coherence is at most 1.1 times the estimates given by (11). The effect of noise on the coherence $\gamma^2(f)$ of (12) is inspected similarly, and the true value is roughly 1.3–1.4 times the estimate given by (12).

6. Results and Discussion

6.1. Background Conditions

[21] The hydrodynamic MTF of (7) and the coherence of (11) were computed for four CoOP time series of about 1 hour each. All of these time series were acquired in the vicinity of Santa Catalina Island, as shown in Figure 2. These results were computed with a minimum and average number of statistical degrees of freedom of 81 and 148, respectively.

[22] Before discussing the MTF results, we summarize the background environmental conditions that may potentially affect the modulation of gravity-capillary waves by gravity waves. First, the time-averaged wave number slope

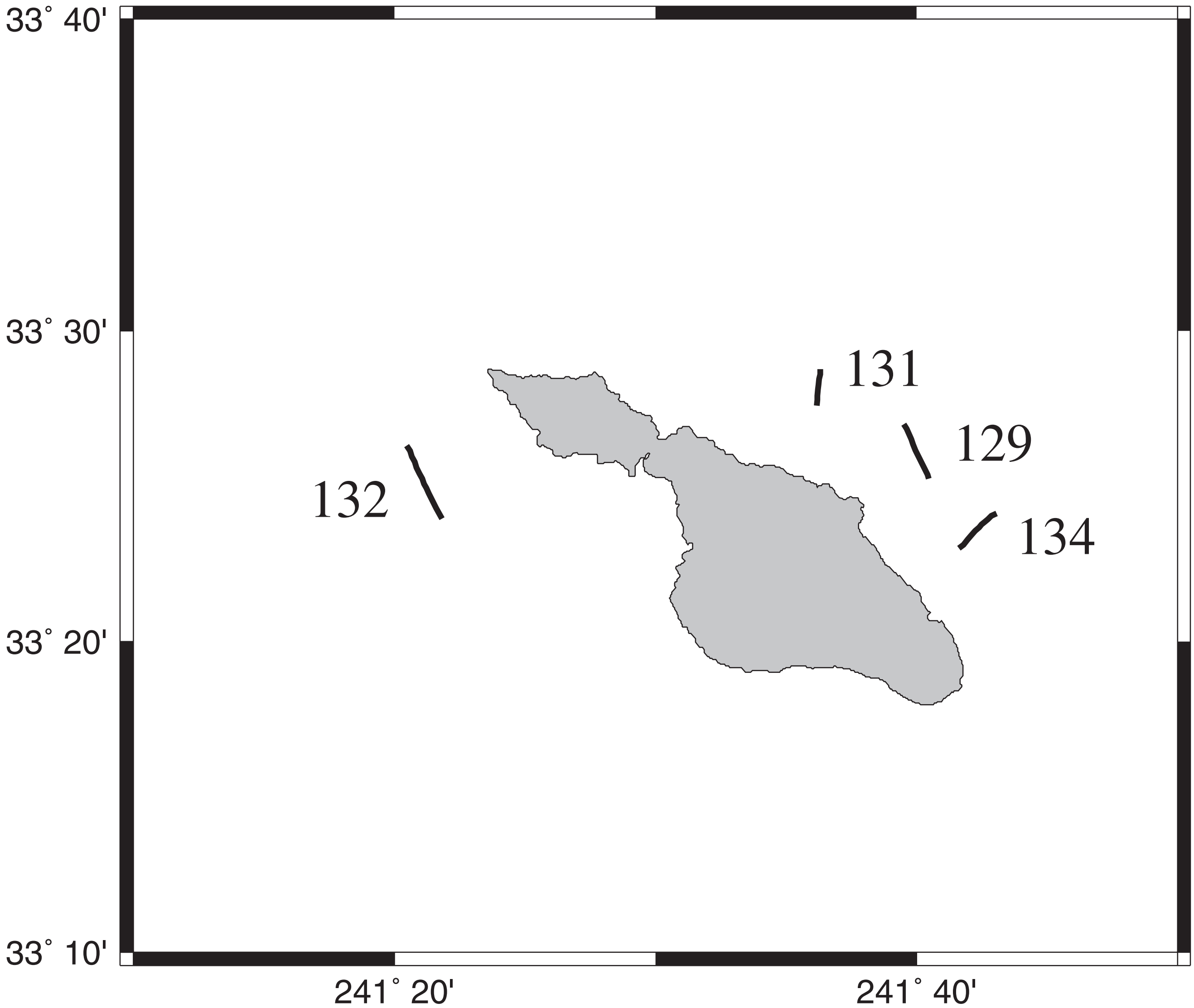

Figure 2. CoOP research catamaran and ship tracks near Santa Catalina Island.

spectra of short wind waves for the four periods are shown in Figure 3. While the wind stress is similar ($u_* = 0.147$–0.158 m s^{-1}) for all four periods, the slope spectrum on Julian Day (JD) 132 is much higher than the rest at higher wave numbers. This is primarily due to very low levels of surface enrichment (indicative of clean surfaces) in the western side of the island, in contrast to higher enrichment levels (indicative of higher surfactant concentrations) in the eastern side [*Hara et al.*, 1998].

[23] The gravity-wave field also varied significantly from day to day. Two characterizations of gravity waves are made: the wave height frequency spectrum and the directional frequency spectrum, with results shown in Figures 4–7. Two versions of the frequency spectrum are computed. One is expressed as a function of intrinsic wave frequency, shown as the solid line in part (a). This spectrum is obtained by integrating the directional frequency spectrum over all propagation angles. The second spectrum is a function of observed frequency, and is shown as the dotted line in part (a). The observed frequencies are Doppler shifted by the motion of the catamaran. The directional frequency spectra shown in part (b) of these figures are computed using the extended DASE method, described in detail by *Hanson et al.* [1997]. The angular distribution of wave energy for the intrinsic frequencies 0.10, 0.15, 0.20, 0.25, and 0.30 Hz are shown.

[24] We first notice that the gravity-wave fields are well developed with low peak frequencies on JD 131 and 132, but are much lower on JD 129 and 134 with higher peak frequencies suggesting fetch-limited conditions. This is most likely due to the sheltering of Santa Catalina Island (see Figure 2) since well-developed swells were consistently propagating from the west during the experimental period. The sheltering effects are also seen in the directionality of the wave spectra. For the results of JD 129 and 132, the wave angle is in rough agreement with the wind direction. On JD 131 and 134, the directional distributions seem to be influenced by the sheltering of Santa Catalina Island. Waves propagating from directions, which intersect the coastline of the island, are fetch limited. The direction of propagation of fetch-limited waves is shown in part (b) as horizontal bars near the top of each figure. The peak directions of the wave

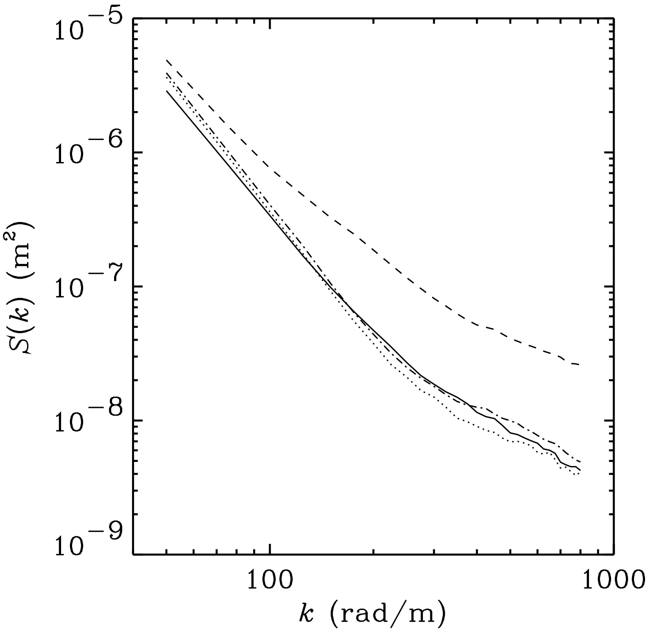

Figure 3. Wave number slope spectrum of short wind waves. Solid line, JD 129; dotted line, JD 131; dashed line, JD 132; dash-dot line, JD 134.

spectra of JD 131 and 134 are located near the edge of the bars rather than near the wind directions.

[25] Background environmental conditions for the four time periods are summarized in Table 1.

6.2. Results of MTF

[26] The coherence levels, MTF magnitudes, and MTF phases are shown for the same four periods in Figures 8–11. In all cases, the coherence values are small, with none above 0.1. The MTF estimates are shown only if the corresponding coherence is above a threshold of 0.04. We choose this threshold since the MTF estimates become substantially noisier when the coherence is below this threshold. The results of JD 129, 131, 132, and 134 have 15, 1, 24, and 7 "above-threshold" coherence values. Each day shows a tendency for the two smallest wave numbers, 50 and 100 rad m^{-1}, to have a larger number of coherence values above 0.04 than for the other wave numbers. Of the total of 47 coherence values above 0.04, 30% and 45% correspond to wave numbers 50 and 100 rad m^{-1}, respectively. Wave numbers 200, 400, and 700 rad m^{-1} contribute only 13%, 9% and 4%.

[27] Let us now examine individual cases separately. The only unlimited fetch condition was met on JD 132. The water surface was clean, and the gravity-wave field was well developed with the dominant frequency of about 0.11 Hz. While the direction of the low-frequency swell was near 90°–100° (eastward), the wave direction at 0.3 Hz was slightly more southward and was better aligned with the wind, suggesting that they were locally generated. Overall, alignment between wind and waves was fair. In Figure 10, the coherence is above 0.04 for a wide range of gravity-wave frequencies at short-wave wave numbers 50 and 100 rad m^{-1}. The MTF magnitude is consistently low around 1–2, and the MTF phase is mostly within ±30°, that is, short-wave spectra are higher near the crest of gravity waves. At wave numbers above 200 rad m^{-1}, the coherence is mostly below 0.04 and only a few MTF values are shown. Both the magnitude and the phase seem to be similar to those at lower wave numbers, although the small number of data makes it difficult to draw any conclusions.

[28] On JD 129, surfactant concentration was higher and the gravity-capillary wave spectrum was much lower than that on JD 132. The gravity-wave field contained no swell components because of the sheltering effect of the island, and locally generated waves were reasonably aligned with the wind with a dominant frequency of about 0.23 Hz. Correspondingly, MTF is observed only above 0.21 Hz in Figure 8. The coherence is reasonably high at all gravity-capillary wave numbers. While the MTF magnitude for wave numbers 50 and 100 rad m^{-1} is around 2–3, that for wave numbers 400 and 700 rad m^{-1} is considerably larger and is scattered around 7–12. The MTF phase is around 10°–70°, suggesting that the short-wave maximum occurs slightly ahead of long-wave crests.

[29] Both on JD 131 and on JD 134 there were almost no locally generated wind waves aligned with wind because of the fetch limitation. On JD 131 significant swell components were observed, while swells were very weak on JD 134. On both days, the swell directions were considerably different (70°–150°) from the wind direction, and the mean short wind wave spectra were low due to surface films. In Figures 9 and 11, one immediately notices that the MTF coherence values are consistently lower than those on JD 129 and 132. This is probably because of the misalignment between the wind direction and the propagation direction of gravity waves. The mechanism of the modulation of short waves by long waves is expected to differ substantially from the aligned to the misaligned cases. In fact, the authors are unaware of any theories predicting modulation when wind and gravity waves are orthogonal to each other. Only a small number of MTF values is obtained, mostly at a short-wave wave number of 100 rad m^{-1}. Both the magnitude and the phase seem to be similar to those on JD 129.

[30] Next, we group together MTF results when wind and waves are roughly aligned (JD 129 and 132), and express them in terms of the normalized wind friction velocity $u_* c^{-1}$, where $c = 2\pi f \kappa^{-1}$ is the phase velocity of the gravity waves. The results are shown in Figure 12 for wave numbers 50 and 100 rad m^{-1}, and in Figure 13 for 200, 400, and 700 rad m^{-1}. These results are distinguished according to their surface enrichment. At wave numbers 50 and 100 rad m^{-1}, the MTF magnitudes are only slightly larger with higher surface enrichment levels compared to those over clean water. At wave numbers above 200 rad m^{-1}, the MTF magnitudes become considerably larger when the surface enrichment level is high. These results are qualitatively consistent with the observation by *Hara and Plant* [1994]. In their study, the hydrodynamic MTF magnitudes estimated using X-band radars (Bragg wave number of about 300 rad m^{-1}) from the Gulf of Mexico are significantly larger than those from the North Sea at lower wind speeds. They speculate that higher concentrations of surface films in the Gulf of Mexico may be responsible for the increased MTF magnitude.

[31] Finally, in Figure 14, we show the hydrodynamic MTF and the coherence calculated with the mean square slope of gravity-capillary waves from both the CoOP and

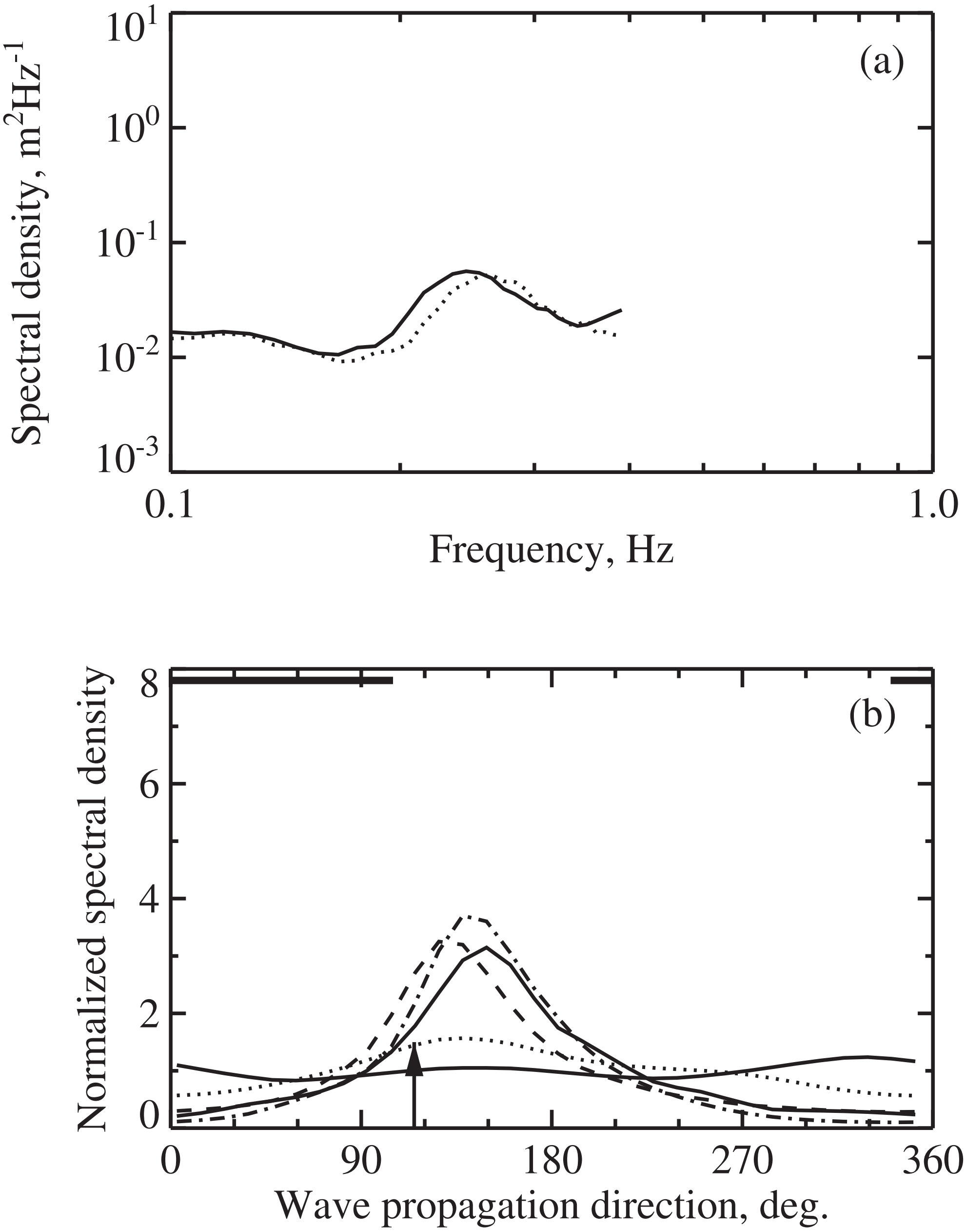

Figure 4. Wave height spectra for JD 129 from 1310 to 1520 GMT. Here, $u_* = 0.150$ m s^{-1} and $U_{10} =$ 4.3 m s^{-1}. (a) Intrinsic frequency (solid) and observed frequency (dotted) spectra. (b) Directional spreading at intrinsic frequencies 0.10 (solid), 0.15 (dotted), 0.20 (dashed), 0.25 (dash-dot), and 0.30 Hz (dash-ellipsis). Horizontal bar at top indicates fetch-limited waves (see text). Arrows indicate wind direction to which wind blows.

High-Res 2 experiments. Again we only show results when wind and waves are roughly aligned. All High-Res 2 results come from a single catamaran deployment on JD 177,since the coherence was lower than 0.04 during all other deployments (JD 168, 173). On JD 177, the wind friction velocity was 0.28 m s^{-1} and gravity waves were well developed with a dominant frequency of 0.11–0.12 Hz. At this high wind stress the effect of surface films on gravity-capillary waves is expected to be weak [*Hara et al.*, 1998]. The MTF results from the two experiments occupy different ranges of the normalized friction velocity, and they appear to complement each other without any significant discrepancies. The MTF magnitude is roughly between 1 and 5 and the MTF phase is roughly between ±70° for the entire wind forcing range. The coherence seems to increase monotonically as the wind forcing increases.

7. Comparison Between Observations and Theoretical Predictions

7.1. Relaxation Theory

[32] In this section, we compare our observations of the hydrodynamic MTF with existing theoretical predictions. Let us assume that there exists a single gravity-wave train

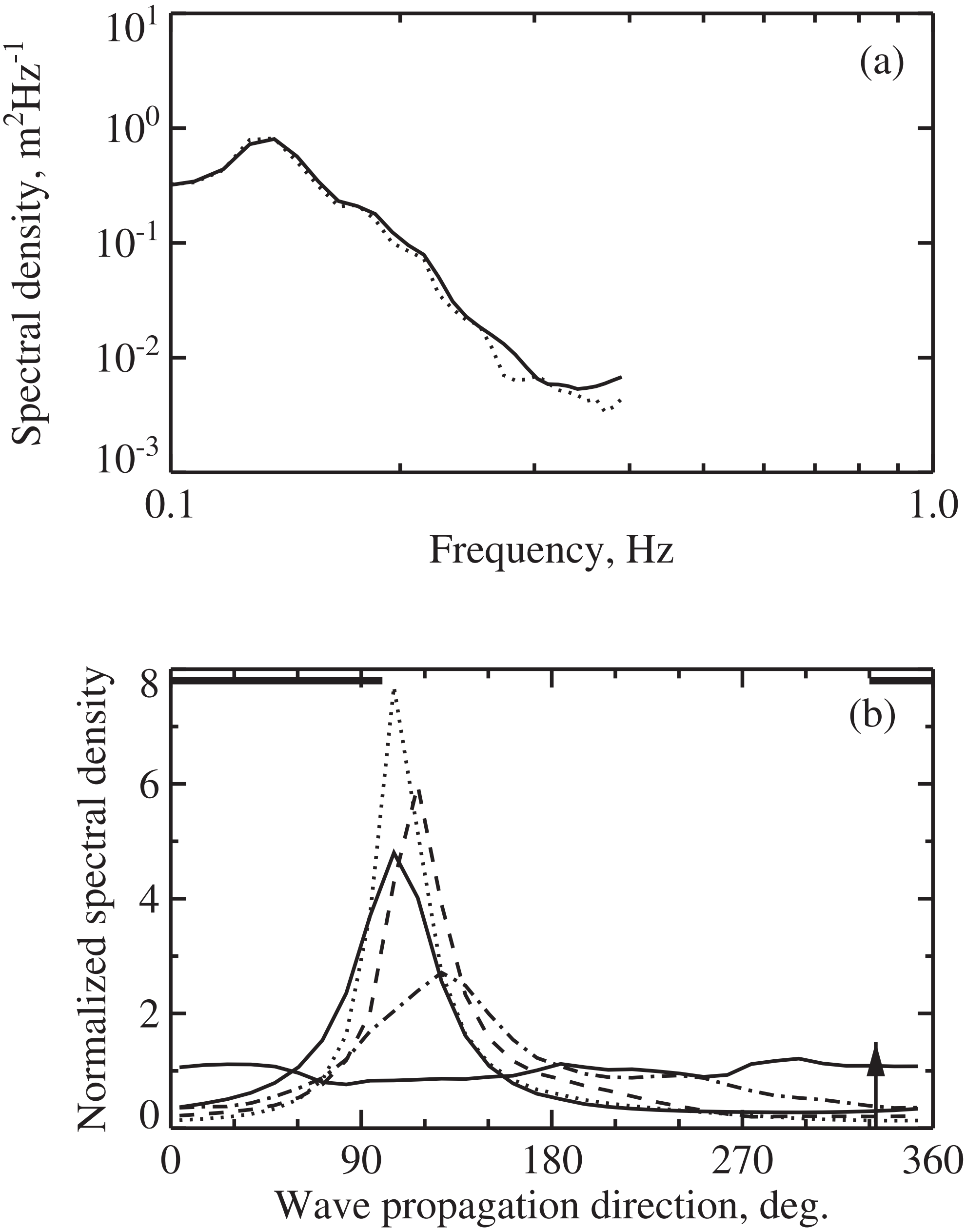

Figure 5. As in Figure 4, but for JD 131 from 0417 to 0552 GMT. Here, $u_* = 0.147$ m s^{-1} and $U_{10} =$ 4.2 m s^{-1}.

with angular frequency σ and wave number κ. From here on we redefine the coordinate system (x, y, z) such that x is the propagation direction of the gravity-wave train and z is vertically upward. In addition to the gravity-wave train, a gravity-capillary wave field exists with a slope spectrum $S(k, \alpha)$, where k is the wave number and α is the propagation direction relative to the x axis. The modulation of the gravity-capillary wave spectrum by the gravity-wave train can be described using the wave action equation

$$\frac{\partial N}{\partial t} + \frac{\partial N}{\partial x}\left(U + \frac{\partial \omega}{\partial k_x}\right) - k_x \frac{\partial N}{\partial k_x}\frac{\partial U}{\partial x} = B \tag{20}$$

[e.g., *Hara and Plant*, 1994]. Here, U is the wave orbital velocity of the gravity-wave train, ω is the angular frequency of gravity-capillary waves, $k_x = k \cos\alpha$ is the x component of the gravity-capillary wave number, and B is the sum of all external forcing terms. For any given (k, α) the forcing B is assumed to be a function of $N(k, \alpha)$ and u_*. The wave action N is related to S such that

$$N(k, \alpha) = \frac{\omega}{k^3} S(k, \alpha). \tag{21}$$

Since the group velocity of the gravity-capillary waves and the orbital velocity of the gravity-wave train are both much smaller than the phase speed of the gravity-wave train, the second term of the left-hand side of (20) is negligibly small compared to the first term.

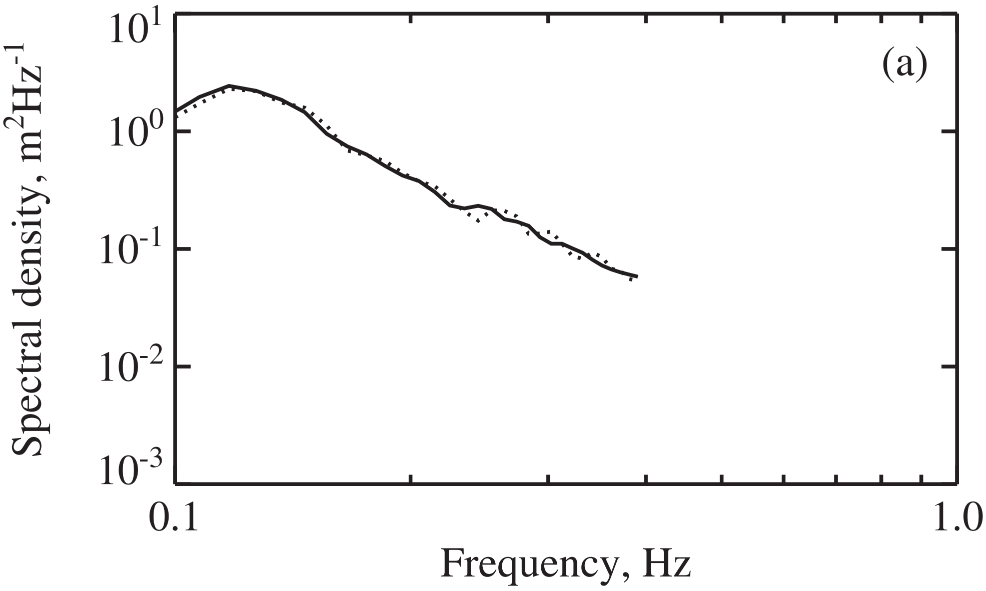

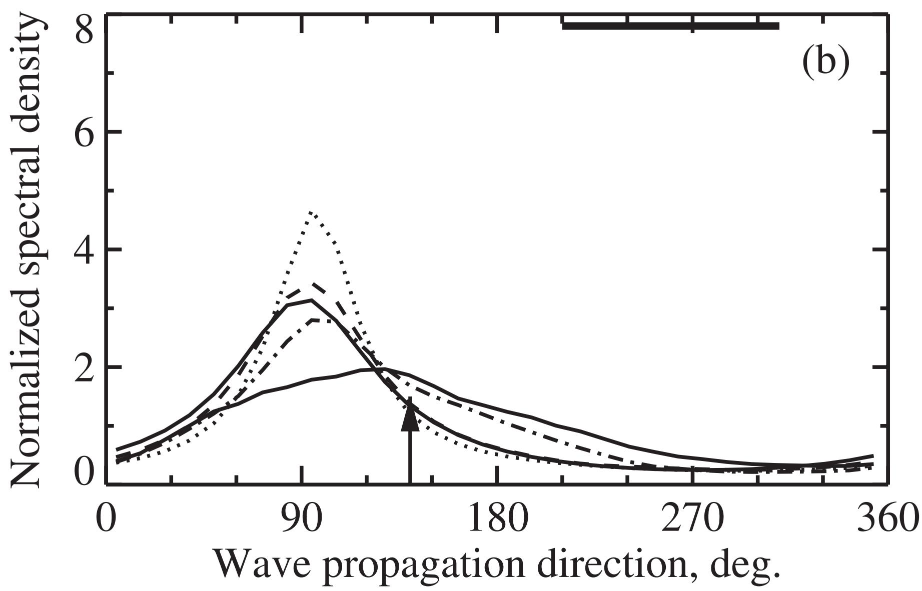

Figure 6. As in Figure 4, but for JD 132 from 1348 to 1637 GMT. Here, $u_* = 0.158$ m s^{-1} and $U_{10} = 4.5$ m s^{-1}.

[33] If the amplitude of the gravity-wave train is sufficiently small, all perturbations due to the gravity-wave train are linearly correlated with the gravity-wave orbital velocity, and we may set

$$U = \tilde{U} e^{-i\kappa x + i\sigma t} \tag{22}$$

$$N(k, \alpha) = \overline{N}(k, \alpha) + \tilde{N}(k, \alpha) e^{-i\kappa x + i\sigma t} \tag{23}$$

and

$$u_* = \bar{u}_* + \tilde{u}_* e^{-i - \kappa x + i\sigma t}, \tag{24}$$

where the overbar denotes time average. Then, the wave action equation for the mean is simply

$$0 = B\left(N = \overline{N}, u_* = \overline{u}_*\right) \tag{25}$$

and the linearized equation for the perturbation is

$$i\sigma\tilde{N} + ik_x\kappa\tilde{U}\frac{\partial\overline{N}}{\partial k_x} = \frac{\partial B}{\partial N}\tilde{N} + \frac{\partial B}{\partial u_*}\tilde{u}_*. \tag{26}$$

Since the mean wave action $\overline{N}$ is expected to be a function of u_* only for any given (k, α), it follows that

$$\frac{\partial B}{\partial N}\frac{\partial\overline{N}}{\partial u_*} + \frac{\partial B}{\partial u_*} = 0. \tag{27}$$

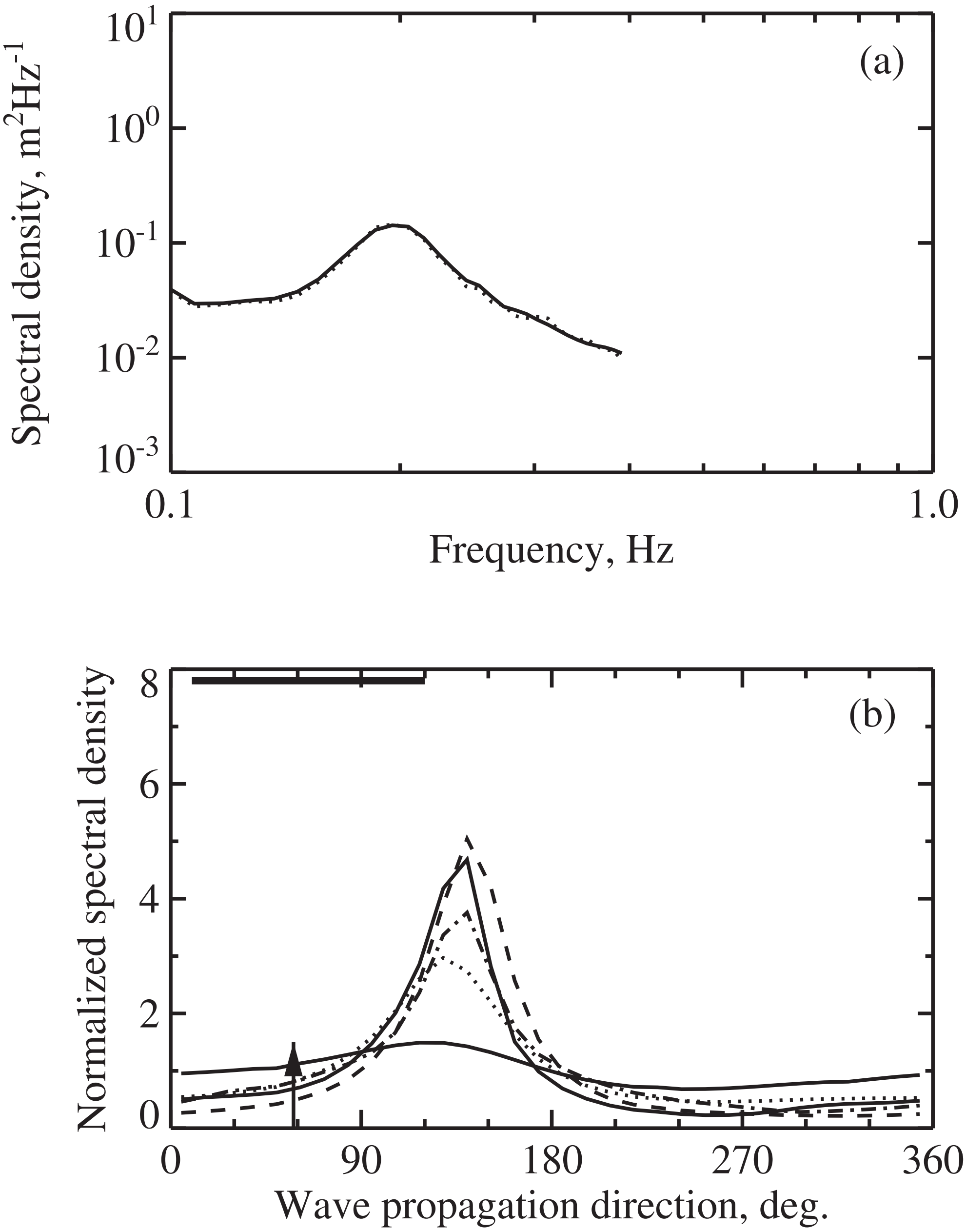

Figure 7. As in Figure 4, but for JD 134 from 0257 to 0452 GMT. Here, $u_* = 0.158$ m s^{-1} and U_{10} = 4.3 m s^{-1}.

Therefore, (26) can be rewritten as

$$i\sigma\tilde{N} + ik_x\kappa\tilde{U}\frac{\partial\overline{N}}{\partial k_x} = -\beta_r\left(\tilde{N} - \frac{\partial\overline{N}}{\partial u_*}\tilde{u}_*\right) \tag{28}$$

where

$$\beta_r = -\frac{\partial B}{\partial N} \tag{29}$$

is often called a relaxation rate. If the forcing term consists of a linear growth term and a nonlinear dissipation term,

$$B = \beta N - \beta_n N^n \tag{30}$$

then it can be shown that

$$\beta_r = (n-1)\beta. \tag{31}$$

Therefore, the relaxation rate β_r is simply equal to β or 2β if the nonlinear dissipation rate is quadratic or cubic [e.g., *Hara and Plant*, 1994].

Table 1. Summary of Conditions for All CoOP Time Series

JD	u_* (m s^{-1})	Surface Enrichment	Dominant Gravity Waves	Angle Between Wind and Waves (°)
129	0.150	high	low	10–40
131	0.147	high	high	130–150
132	0.158	low	high	10–50
134	0.158	high	low	70–90

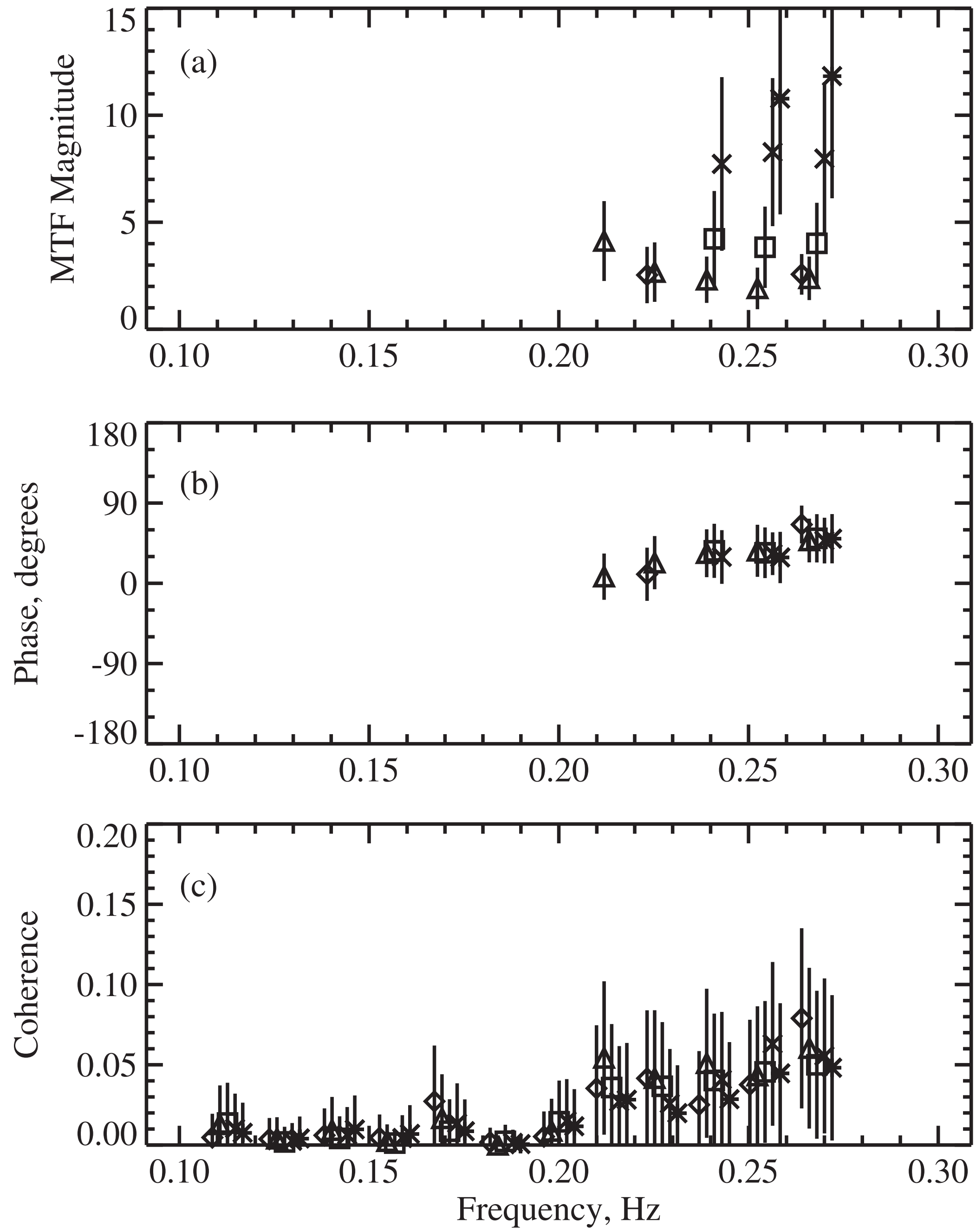

Figure 8. Hydrodynamic MTF and coherence for JD 129 from 1310 to 1520 GMT. Diamonds, $k = 50$ rad m^{-1}; triangles, 100 rad m^{-1}; squares, 200 rad m^{-1}; crosses, 400 rad m^{-1}; asterisks, 700 rad m^{-1}. For clarity, symbols corresponding to increasing k are incrementally offset to the right. Vertical bars are 95% confidence levels. (a) MTF magnitude. (b) MTF phase. (c) Coherence.

[34] We may now solve (28) for $\tilde{N}$ as

$$\tilde{N}(k,\alpha) = \left(1 - i\frac{\beta r}{\sigma}\right)^{-1}\left(-\frac{\tilde{U}}{c}k_x\frac{\partial\overline{N}}{\partial k_x} - i\frac{\beta_r}{\sigma}\frac{\partial\overline{N}}{\partial u_*}\tilde{u}_*\right) \quad (32)$$

Furthermore, if we set

$$S(k,\alpha) = \overline{S}(k,\alpha) + \tilde{S}(k,\alpha)e^{-i\kappa x + i\sigma t} \quad (33)$$

and express $\partial/\partial k_x$ in terms of $\partial/\partial k$ and $\partial/\partial\alpha$, (32) can be rewritten for $\tilde{S}$ as

$$\tilde{S}(k,\alpha) = \left(1 - i\frac{\beta_r}{\sigma}\right)^{-1}\left[-\frac{\tilde{U}}{c}\left(k\frac{\partial\overline{S}}{\partial k} + \frac{k}{\omega}\frac{\partial\omega}{\partial k}\overline{S} - 3\overline{S}\right)\cos^2\alpha + \frac{\tilde{U}}{c}\frac{\partial\overline{S}}{\partial\alpha}\cos\alpha\ \sin\alpha - i\frac{\beta_r}{\sigma}\frac{\partial\overline{S}}{\partial u_*}\tilde{u}_*\right] \quad (34)$$

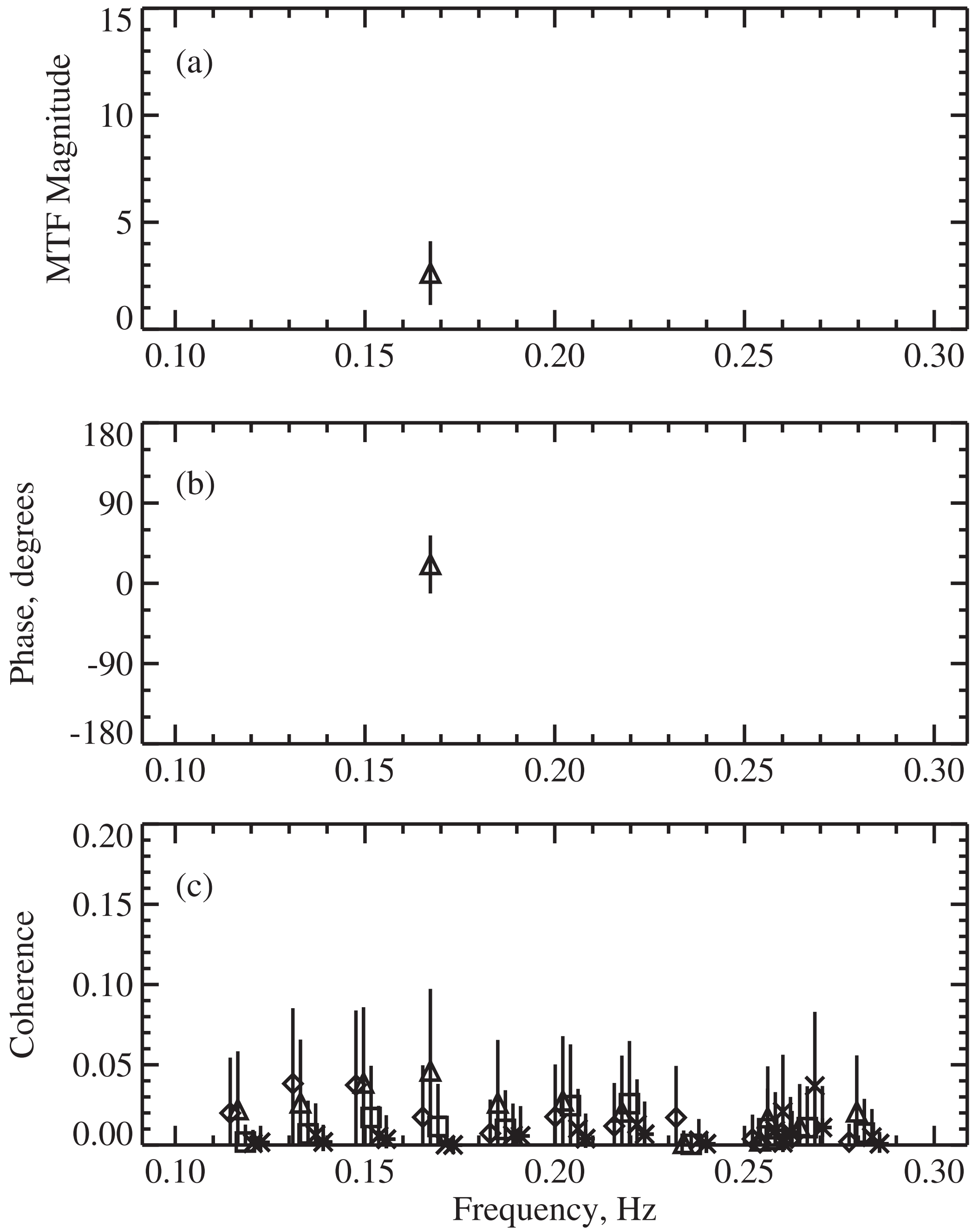

Figure 9. As in Figure 8, but for JD 131 from 0417 to 0552 GMT.

with $c = \sigma/\kappa$. Integrating in all angles,

$$S(k) = \overline{S}(k) + \tilde{S}(k)e^{-i\kappa x + i\sigma t} \tag{35}$$

with

$$\overline{S}(k) = \int_{-\pi/2}^{\pi/2} \overline{S}(k,\alpha)d\alpha, \qquad \tilde{S}(k) = \int_{-\pi/2}^{\pi/2} \tilde{S}(k,\alpha)d\alpha. \tag{36}$$

Finally, these results are introduced to our definition of the hydrodynamic MTF, yielding

$$\begin{aligned} M(f,k) &= \frac{1}{\kappa \overline{S}(k)} \frac{C_{S\eta}(k,f)}{C_{\eta\eta}(f)} = \frac{c}{\overline{S}(k)} \frac{\tilde{S}(k)}{\tilde{U}} \\ &= \left(\int_{-\pi/2}^{\pi/2} \overline{S}(k,\alpha)d\alpha \right)^{-1} \frac{c}{\tilde{U}} \int_{-\pi/2}^{\pi/2} \tilde{S}(k,\alpha)d\alpha \\ &= \left(\int_{-\pi/2}^{\pi/2} \overline{S}(k,\alpha)d\alpha \right)^{-1} \int_{-\pi/2}^{\pi/2} \left(1 - i\frac{\beta_r}{\sigma}\right)^{-1} \\ &\quad \times \left[-\left(k\frac{\partial \overline{S}}{\partial k} + \frac{k}{\omega}\frac{\partial \omega}{\partial k}\overline{S} - 3\overline{S} \right) \cos^2\alpha \right. \\ &\quad \left. + \frac{\partial \overline{S}}{\partial \alpha} \cos\alpha \sin\alpha - i\frac{\beta_r}{\sigma} c \frac{\partial \overline{S}}{\partial u_*} \frac{\tilde{u}_*}{\tilde{U}} \right] d\alpha. \end{aligned} \tag{37}$$

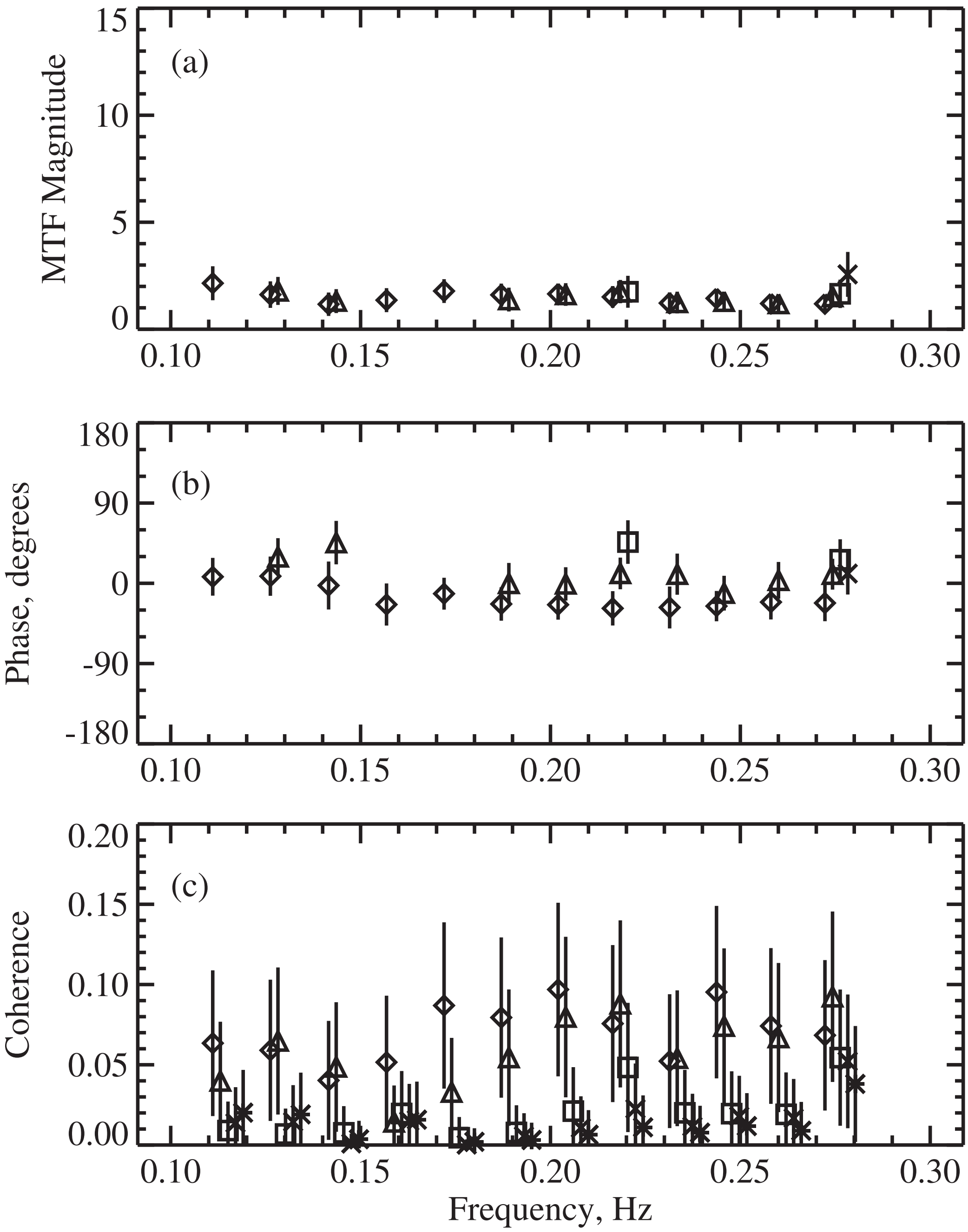

Figure 10. As in Figure 8, but for JD 132 from 1348 to 1637 GMT.

Therefore, in order to evaluate $M(f, t)$ we have to know the value of β_r, the exact shape of $\overline{S}(k, \alpha)$ and its dependence on u_*, as well as the modulation of the wind friction velocity $\tilde{U}_*/\tilde{U}$.

[35] Let us assume that the mean wave number slope spectrum $\overline{S}$ can be (locally) approximated in the form of

$$\overline{S} = S_0\, u_*^{n_3} k^{-n_1} \cos^{n_2} \alpha. \tag{38}$$

Introducing this into (37) yields

$$M(f,k) = \left(\int_{-\pi/2}^{\pi/2} \cos^{n_2}\alpha\, d\alpha\right)^{-1} \int_{-\pi/2}^{\pi/2} \left(1 - i\frac{\beta_r}{\sigma}\right)^{-1} \times \left[\left(n_1 - \frac{k}{\omega}\frac{\partial\omega}{\partial k} + 3\right)\cos^2\alpha - n_2 \sin^2\alpha - i\frac{\beta_r}{\sigma} n_3 M_u\right] \cos^{n_2}\alpha\, d\alpha \tag{39}$$

with

$$M_u = \frac{c}{\overline{u}_*}\frac{\tilde{u}_*}{\tilde{U}}. \tag{40}$$

For $\beta_r/\sigma \ll 1$, $M(f, k)$ approaches to

$$M(f,t) \simeq \left(\int_{-\pi/2}^{\pi/2} \cos^{n_2}\alpha d\alpha\right)^{-1} \cdot \int_{-\pi/2}^{\pi/2}\left[\left(n_1 - \frac{k}{\omega}\frac{\partial\omega}{\partial k} + 3\right)\cos^2\alpha - n_2\sin^2\alpha\right]\cos^{n_2}\alpha\, d\alpha. \tag{41}$$

Therefore, the phase of the MTF is zero and its magnitude is determined by the two parameters n_1 and n_2 only. For

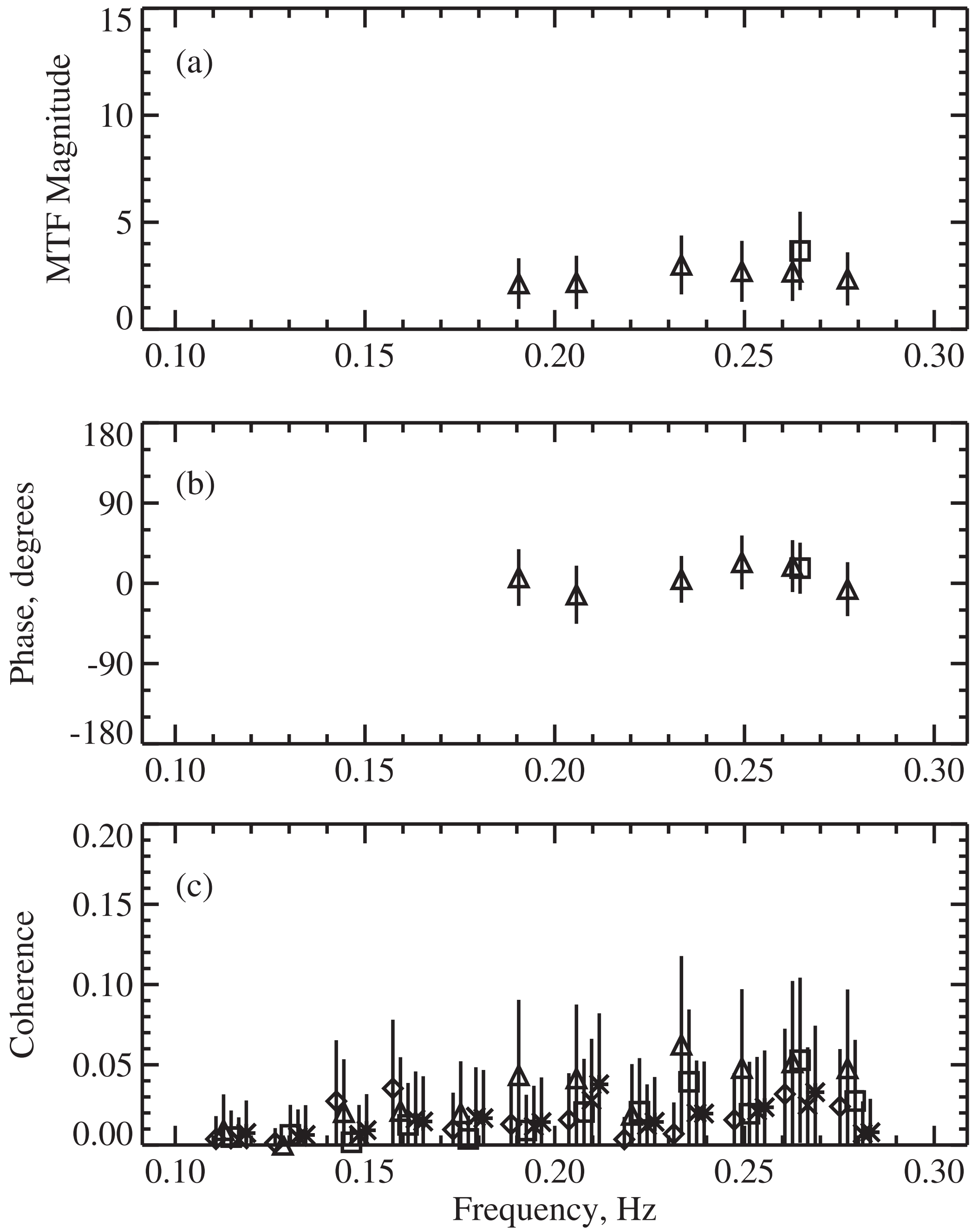

Figure 11. As in Figure 8, but for JD 134 from 0257 to 0452 GMT.

$\beta_r/\sigma \gg 1$, $M(f, k)$ approaches to n_3M_u, which depends on how the mean gravity-capillary wave spectrum varies with the wind stress and how the wind stress varies along the phase of the gravity-wave train. Although the wind modulation M_u has never been observed directly, *Smith* [1986] estimates that the phase of M_u is zero and its magnitude is about 10. *Hara and Plant* [1994] estimate that at the Bragg wave number of about 300 rad m^{-1} the phase of n_3M_u is close to zero and its magnitude decreases from about 10 to about 3 as the wind speed increases from 5 to 15 m s^{-1}.

7.2. Comparison With CoOP Observations

[36] We now evaluate the theoretical estimate of the hydrodynamic MTF using (39) for JD 129 and JD 132 during the CoOP experiment, when wind and dominant gravity waves were roughly aligned. The parameters n_1, n_2, and n_3 have been estimated directly from the observed mean wave spectrum [*Hara et al.*, 1998] and are shown in Table 2. The relaxation rate β_r is simply set to be equal to the growth rate,

$$\beta_r = 0.04 \frac{u_*^2 k^2}{\omega} \cos^2 \alpha \tag{42}$$

and M_u is set to be either 0 or 5; the latter is about half the value suggested by *Smith* [1986] and yields values of n_3M_u that are roughly consistent with the estimates by *Hara and*

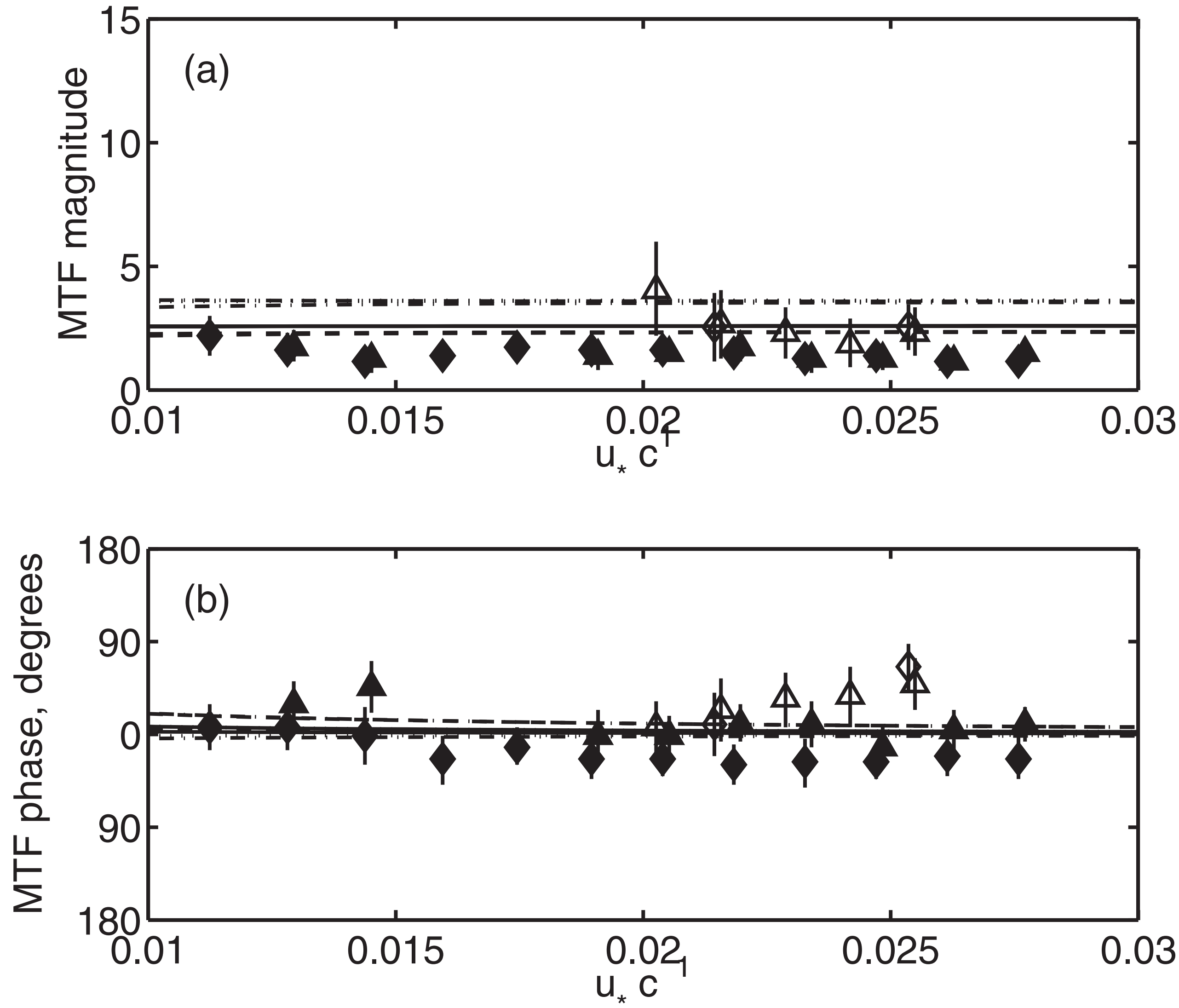

Figure 12. Hydrodynamic MTF from JD 129 and 132 for gravity-capillary wave number k = 50 (diamond) and 100 rad m^{-1} (triangle) and for low (closed) and high (open) values of surface enrichment. For clarity, symbols corresponding to increasing k are incrementally offset to the right. Theoretical estimates are shown by solid line (k = 50 rad m^{-1}, low surface enrichment), dashed line (k = 100 rad m^{-1}, low surface enrichment), dotted line (k = 50 rad m^{-1}, high surface enrichment), and dash-dot line (k = 100 rad m^{-1}, high surface enrichment).

Plant [1994]. The results are plotted in Figures 12 and 13. In all cases, the results with M_u = 5 show larger MTF magnitude and larger MTF phase than with M_u = 0.

[37] At lower gravity-capillary wave numbers (k = 50 and 100 rad m^{-1}), the relaxation rate β_r is much smaller than the gravity-wave angular frequency σ. Hence, the results are little affected by the choice of M_u. The overall agreement between the theory and the observation is reasonable. The theory correctly predicts that the magnitude of MTF is larger when surface films are present, although the theory slightly overpredicts the MTF magnitude for all cases. At higher wave numbers (k = 200 and 400 rad m^{-1}), the theoretical values differ significantly depending on the choice of M_u. As M_u increases from 0 to 5, the MTF amplitude and phase both increase, and the overall agreement between the theory and the observations improves. With M_u = 5 the MTF magnitude and phase are both accurately predicted for all cases.

[38] We have also evaluated the MTF using (39) with the relaxation rate being twice the growth rate. The results are slightly modified but the overall agreement between the observations and the theory remains similar. In summary, we may conclude that the existing relaxation theory may predict the hydrodynamic MTF that is roughly consistent with observations if proper choice of M_u is made. It is noteworthy that the effect of the modulated wind stress is significant even at such low wind stress (u_* = 0.150–0.158 m s^{-1}) encountered during CoOP. The reasonable agreement between the observations and the theory further confirms that the presence of surfactants may significantly

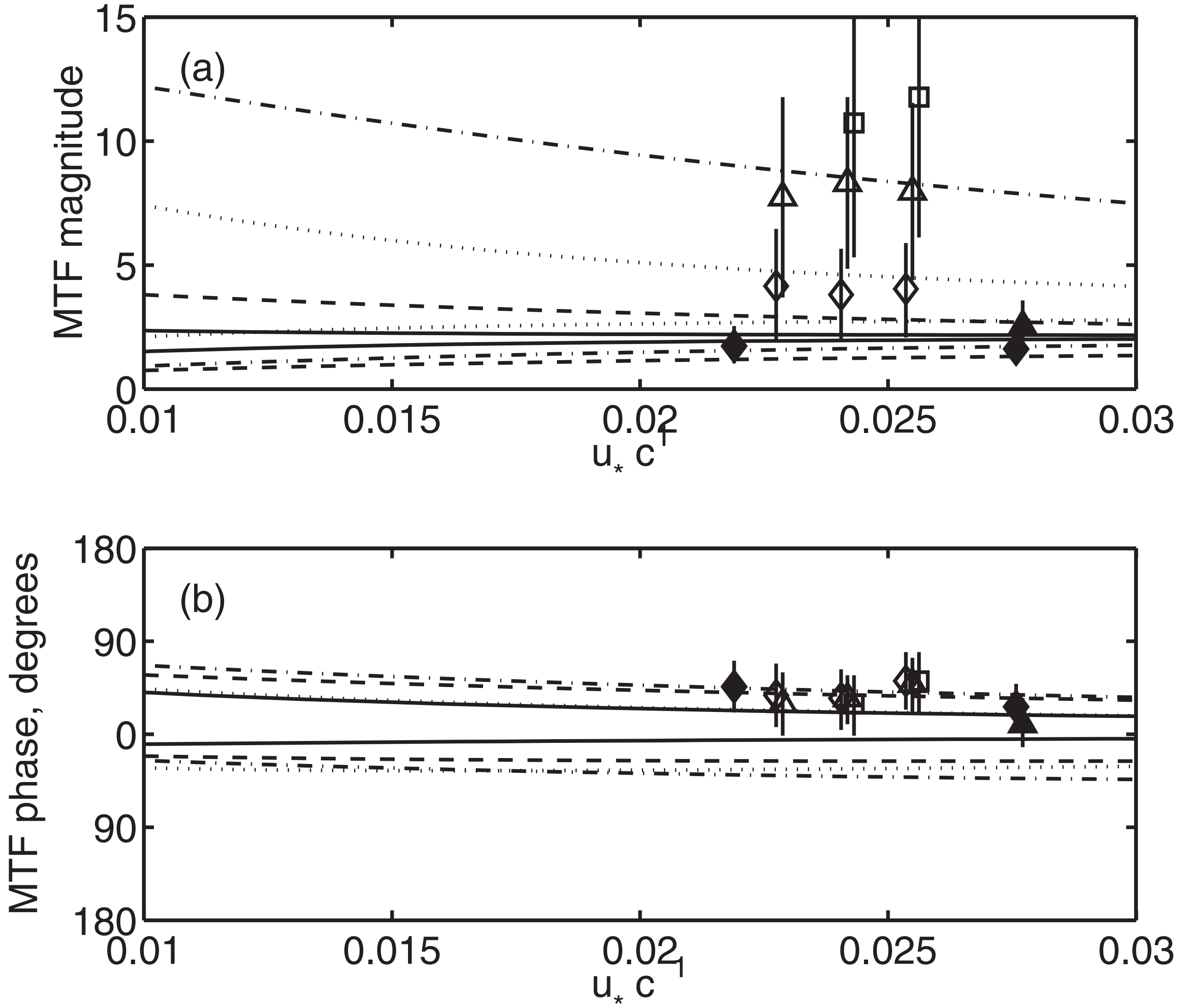

Figure 13. As in Figure 12, but for gravity-capillary wave number k = 200 (diamond), 400 (triangle), and 700 rad m^{-1} (square). Theoretical estimates are shown by solid line (k = 200 rad m^{-1}, low surface enrichment), dashed line (k = 400 rad m^{-1}, low surface enrichment), dotted line (k = 200 rad m^{-1}, high surface enrichment), and dash-dot line (k = 400 rad m^{-1}, high surface enrichment).

modify the hydrodynamic MTF. This is mainly because the short wave spectrum increases faster with u_* (i.e., n_3 is larger) with higher concentrations of surfactants.

8. Concluding Remarks

[39] Using a SLSG, a wave wire array, and a motion detection package mounted on a research catamaran, we have estimated the hydrodynamic MTF without relying on microwave radar observations. Most of the observations have been made under low wind conditions. The observed coherence is generally below 0.1, suggesting that the modulation of short wind waves is not strongly correlated with dominant gravity waves. The coherence is slightly higher for wave numbers 50–100 rad m^{-1} than for wave numbers above 200 rad m^{-1}. When wind and dominant waves are not aligned, the coherence becomes even lower. When waves are aligned with wind and the water surface is clean, the magnitude of the hydrodynamic MTF is around 2–4 and its phase is close to 0. When surfactant concentration is higher, the MTF magnitudes are only slightly larger at wave numbers 50–100 rad m^{-1} but are significantly larger at wave numbers above 200 rad m^{-1}. The results from the two field experiments appear to be roughly consistent with each other.

[40] We have compared our observed hydrodynamic MTF with the theoretical predictions using the existing relaxation theory. The theory may predict the hydrodynamic MTF values that are roughly consistent with observations if the effect of modulated wind stress over long waves is included.

[41] One of the significant findings of this study is that the correlation between the dominant gravity waves and the modulation of short wind waves is very weak at low wind speeds. In fact, there seems to be no statistically significant correlation between long gravity waves (frequency less than 0.2 Hz) and very short wind waves (wave number above

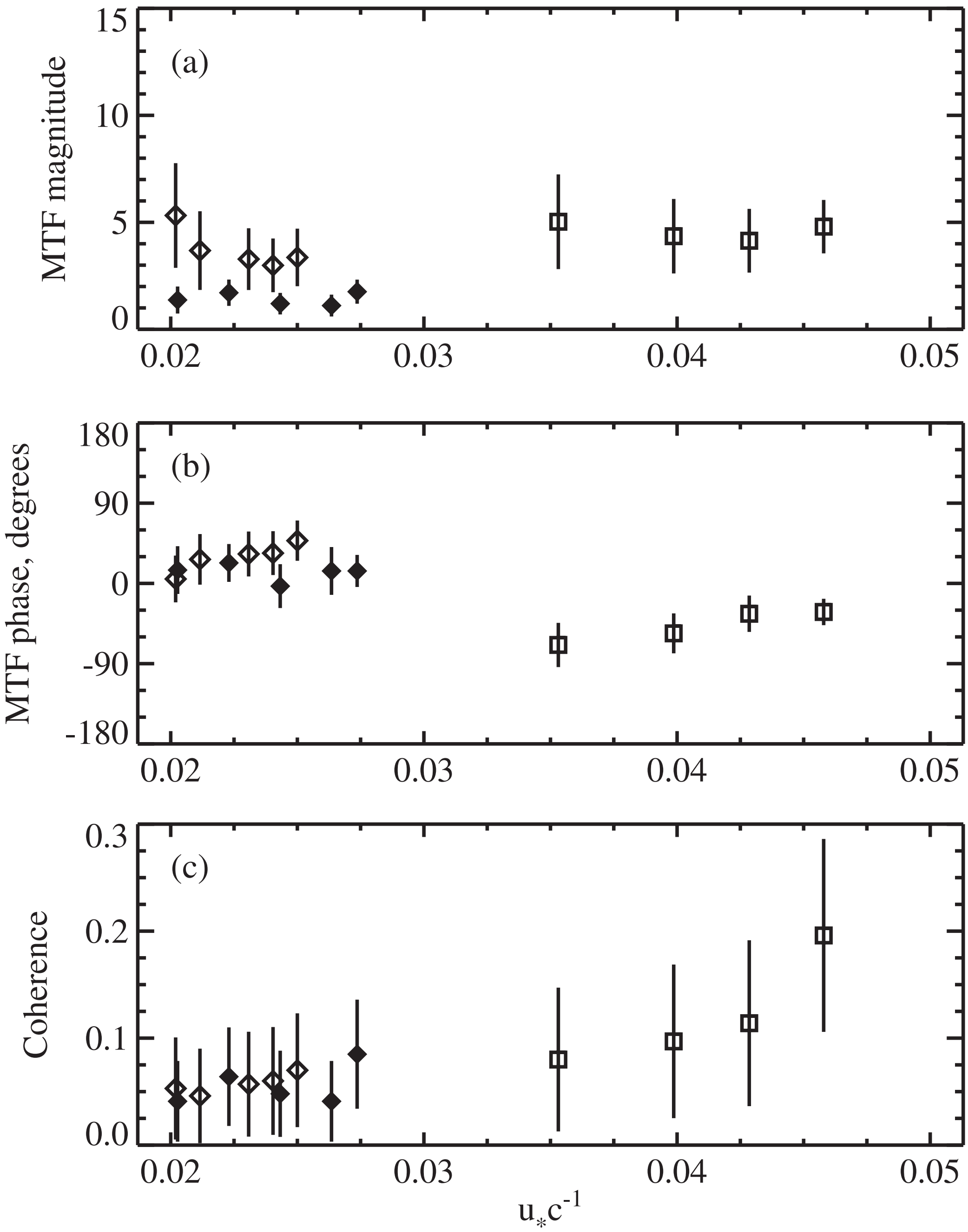

Figure 14. Hydrodynamic MTF and coherence of mean square slope of gravity-capillary waves for CoOP (diamond) and High-Res 2 (square) experiments. Low (closed) and high (open) values of surface enrichment are indicated for CoOP only.

200 rad m^{-1}) in the conditions we have encountered. This result may have significant implications to various microwave remote sensing techniques that rely on the hydrodynamic MTF. It also implies that wind gustiness (or some other external environmental condition) is responsible for most of the variability of short wind wave spectra.

[42] Because of the very limited amount of data and large error bars, the results in this study are at most tentative. Further studies are needed to improve our understanding of the modulation of short wind waves by dominant gravity waves.

Table 2. Coefficients n_1, n_2, and n_3

	k (rad m^{-1})	50	100	200	400
JD 129	n_1	3	3	2.3	1.6
	n_2	2	2	2	2
	n_3	1	1	2.4	3
JD 132	n_1	2.7	2.3	2	1.4
	n_2	0	0	0	0
	n_3	0.5	0.5	0.8	1.2

[43] **Acknowledgments.** We thank James Edson and Wade McGillis of Woods Hole Oceanographic Institution for providing the meteorological data. This research was supported by ONR grant N00014-93-11214. Additional support was provided by ONR grants N00014-96-1-0510 (TH) and N00014-96-1-0516 (EJB).

References

Alpers, W., and K. Hasselmann, The two-frequency microwave technique for measuring ocean-wave spectra from an airplane or satellite, *Boundary Layer Meteorol.*, *13*, 215–230, 1978.

Bock, E. J., and T. Hara, Optical measurements of capillary-gravity wave spectra using a scanning laser slope gauge, *J. Atmos. Oceanic Technol.*, *12*, 395–403, 1995.

Bock, E. J., et al., Description of the science plan for the April 1995 CoOP experiment, "Gas Transfer in Coastal Waters," performed from the Research Vessel *New Horizon*, in *Air–Water Gas Transfer*, edited by B. Jähne and E. C. Monahan, pp. 801–810, Aeon-Verlag, Hanau, Germany, 1995.

Fairall, C. W., E. F. Bradley, D. P. Rodgers, J. B. Edson, and G. S. Young, Bulk parameterization of air–sea fluxes for Tropical Ocean-Global Atmosphere Coupled-Ocean Atmosphere Response Experiment, *J. Geophys. Res.*, *101*, 3747–3764, 1996.

Hanson, K. A., T. Hara, E. J. Bock, and A. B. Karachintsev, Estimation of directional surface wave spectra from a towed research catamaran, *J. Atmos. Oceanic Technol.*, *14*, 1467–1482, 1997.

Hara, T., and W. J. Plant, Hydrodynamic modulation of short wind-wave spectra by long waves and its measurement using microwave backscatter, *J. Geophys. Res.*, *99*, 9767–9784, 1994.

Hara, T., E. J. Bock, J. B. Edson, and W. R. McGillis, Observations of short wind waves in coastal waters, *J. Phys. Oceanogr.*, *28*, 1425–1438, 1998.

Hauser, D., and G. Caudal, Combined analysis of the radar cross-section modulation due to the long ocean waves around 14° and 34° incidence: Implication for the hydrodynamic modulation, *J. Geophys. Res.*, *101*, 25,833–25,846, 1996.

Keller, W. C., and J. W. Wright, Microwave scattering and the straining of wind-generated waves, *Radio Sci.*, *10*, 139–147, 1975.

Kudryavtsev, V. N., C. Mastenbroek, and V. K. Makin, Modulation of wind ripples by long surface waves via the air flow: A feedback mechanism, *Boundary Layer Meteorol.*, *83*, 99–116, 1997.

Plant, W. J., The modulation transfer function: Concept and applications, in *Radar Scattering From Modulated Wind Waves*, edited by G. J. Komen and W. A. Oost, pp. 155–172, Kluwer Acad., Norwell, Mass., 1989.

Romeiser, R., and W. Alpers, An improved composite surface model for the radar backscattering cross section of the ocean surface, 2, Model response to surface roughness variations and the radar imaging of underwater bottom topography, *J. Geophys. Res.*, *102*, 25,251–25,267, 1997.

Romeiser, R., A. Schmidt, and W. Alpers, A three-scale composite surface model for the ocean wave-radar modulation transfer function, *J. Geophys. Res.*, *99*, 9785–9801, 1994.

Smith, J., Short surface waves with growth and dissipation, *J. Geophys. Res.*, *91*, 2616–2632, 1986.

Wright, J. W., W. J. Plant, and W. C. Keller, Ocean wave-radar modulation transfer functions from the West Coast Experiment, *J. Geophys. Res.*, *85*, 4957–4966, 1980.

E. J. Bock, Interdisciplinary Center for Scientific Computing, IWR, University of Heidelberg, Heidelberg, Germany.

K. A. Hanson, T. Hara, and B. Mete Uz, Graduate School of Oceanography, University of Rhode Island, Narragansett, RI 02882, USA. (thara@uri.edu)